LA-UR-14-25213
Approved for public release; distribution is unlimited.

Title: Simulation of xenon, uranium vacancy and interstitial diffusion and grain boundary segregation in UO2

Author(s): Andersson, Anders D.
Tonks, Michael R.
Casillas, Luis
Nerikar, Pankaj
Vyas, Shyam
Uberuaga, Blas P.
Stanek, Christopher R.

Intended for: Report

Issued: 2014-10-31 (rev.1)

Simulation of xenon, uranium vacancy and interstitial diffusion and grain boundary segregation in UO_2

David A. Andersson,[1] Michael R. Tonks,[2] Luis Casillas,[1] Pankaj Nerikar,[1] Shyam Vyas,[1] Blas P. Uberuaga,[1] and Christopher R. Stanek[1]

[1] *Materials Science and Technology Division, Los Alamos National Laboratory, Los Alamos, NM 87545*
[2] *Fuel Modeling and Simulation, Idaho National Laboratory, P.O. Box 1625, Idaho Falls, ID 83415*

In light water reactor fuel, gaseous fission products segregate to grain boundaries, resulting in the nucleation and growth of large intergranular fission gas bubbles. Based on the mechanisms established from density functional theory (DFT) and empirical potential calculations[1], continuum models for diffusion of xenon (Xe), uranium (U) vacancies and U interstitials in UO_2 have been derived for both intrinsic conditions and under irradiation. Segregation of Xe to grain boundaries is described by combining the bulk diffusion model with a model for the interaction between Xe atoms and three different grain boundaries in UO_2 ($\Sigma5$ tilt, $\Sigma5$ twist and a high angle random boundary), as derived from atomistic calculations. All models are implemented in the MARMOT phase field code, which is used to calculate effective Xe and U diffusivities as well as redistribution for a few simple microstructures.

I. INTRODUCTION

In UO_2 nuclear fuel, the retention and release of fission gas atoms such as xenon (Xe) are important aspects of overall fuel performance. For example, the formation of fission gas bubbles induces fuel swelling, which contributes to mechanical interaction with the clad thereby increasing the probability of clad breach. Fission gas bubbles also decrease the thermal conductivity of the fuel. Alternatively, fission gas can be released from the fuel to the plenum. This increases the pressure on the clad walls. In order to predict the fuel performance as function of burn-up, the redistribution of fission gas atoms must be understood[35]. Most fission gases have low solubility in the fuel matrix, which is especially pronounced for large fission gas atoms such as Xe. As a result there is a significant driving force for segregation of gas atoms to extended defects, e.g. grain boundaries and dislocations, and subsequently for nucleation of gas bubbles at these sinks. After segregating to grain boundaries fission gases may be released to the fuel plenum, either by fast diffusion of individual gas atoms along grain boundaries or by interlinked gas bubbles forming percolation networks.

Several empirical or semi-empirical models have been developed for fission gas release in nuclear fuels, e.g. Refs. 2–7. One of the most commonly used models in fuel performance codes was published by Massih and Forsberg[4,5,7]. This model is similar to the early Booth model[2] in that it applies an equivalent sphere to separate bulk UO_2 from grain boundaries represented by the circumference. Compared to the Booth model, it also captures trapping at grain boundaries, fission gas resolution and describes release from the boundary by applying time-dependent boundary conditions to the circumference. In this and most other release models the fission gas diffusion rates are taken from the analysis of Turnbull[23], which captures both intrinsic and radiation enhanced diffusion. In order to provide more detailed insight into the role of microstructure, several authors have applied phase field models to simulate evolution of fission gases and related properties in nuclear fuels [11–17]. Others approach the same problem using rate theory models[8–10].

The success of phase field and other meso-scale models to capture the evolution of fission gases relies on an accurate representation of the underlying atomistic mechanisms and accurate parameterization of the driving forces and kinetics for these mechanisms. Even though effective diffusivities under specific conditions may be derived from integrated fission gas annealing experiments, it is very difficult to obtain information regarding the underlying atomistic mechanisms. For this reason, we rely on detailed mechanisms and data determined from density functional theory (DFT) and atomistic calculations[18,19,22] to derive models for Xe, uranium (U), uranium vacancy (Va) and uranium interstitial (U_I) diffusion as well as for segregation to grain boundaries in UO_2. These models apply concepts from both classical reaction rate theory and from phase field theory. The MARMOT phase field code[25–27] is used to estimate effective Xe and U diffusivities under both intrinsic and different irradiation conditions as well as to simulate the fission gas evolution for a few simple microstructures. This work is motivated as a step towards developing meso-scale models for simulating high burnup structures.

II. XE, U VACANCY AND U INTERSTITIAL DIFFUSION MODELS

A. Model derivation

The redistribution of Xe, U vacancies and U interstitials may be described by diffusion equations:

$$\frac{\partial y_X}{\partial t} = \nabla \cdot (D_X \nabla y_X)\,, \tag{1}$$

where X denotes either Xe, U vacancies or U interstitials, y_X is the corresponding concentration (fractional)

and D_X the effective diffusivity, which is a function of, e.g., the species concentration, irradiation conditions, microstructure and temperature. In order to accurately express the diffusivities as function of these parameters, we develop models that capture the mechanistic aspects of diffusion.

DFT and empirical potential calculations have shown that Xe atoms occupy U vacancy trap sites, which may also include oxygen vacancies depending on the $UO_{2\pm x}$ (non-)stoichiometry[1,19,21,30]. In this study we assume nearly stoichiometric UO_2, for which the preferred trap site is a U vacancy coordinated with one oxygen (O) vacancy (Xe_{UO})[1,19,21,30]. The charge state of this cluster (the number of bound holes) is also important and for stoichiometric UO_2 it is fully charged (no bound holes, Xe''_{UO} in modified Kröger-Vink notation)[1]. O defects or ions will not be explicitly treated in this study, since their dynamics are many orders of magnitude faster than for Xe atoms and U ions, which implies that the O defect concentration can be assumed to fulfill equilibrium conditions. The same conclusion applies to electronic defects. The Xe_{UO} cluster is not mobile due to the high migration barrier associated with cation exchange mechanisms, but diffusion rather occurs by binding another U vacancy to the trap site, which in stoichiometric UO_2 creates a cluster denoted Xe_{U_2O} (Xe occupying a trap site consisting of two U vacancies and one O vacancy, which is fully charged, Xe'''''_{U_2O} in Kröger-Vink notation). There are two limits for the effective mobility of this cluster. If the binding energy of the U vacancy to the trap site is low and the intracluster vacancy barrier is high, the mobility is given by the bulk migration properties of U vacancies. On the other hand, if the binding energy is high and the intracluster barrier is low, then the mobility is given by the cluster migration properties. The latter case is active if

$$G_M^{V_U} > G_M^{V_U^C} + G_B^{V_U}, \tag{2}$$

where $G_M^{V_U}$ is the bulk vacancy migration barrier, $G_M^{V_U^C}$ the intracluster vacancy migration barrier and $G_B^{V_U}$ the binding energy of vacancies to the Xe trap site. DFT and empirical potential calculations of the migration and binding properties have established that for Xe the above condition is always fulfilled, i.e. the mobility is given by the cluster migration properties. The Xe atom can easily move between the two vacancies of the mobile cluster, because it has a low migration barrier compared to both $G_M^{V_U}$ and $G_M^{V_U^C}$, which explains why the rate limiting step for Xe_{U_2O} cluster diffusion is migration of one of the U vacancies to a next nearest site ($G_M^{V_U^C}$). This is equivalent to the cluster diffusing via an exchange mechanism involving two uranium atoms. For additional details, see Refs. 1 and 19.

Based on this mechanism, the Xe diffusivity is expressed as ($y_{Xe}^{TOT} = y_{Xe_U} + y_{Xe_{U_2O}}$):

$$\begin{aligned} \frac{\partial y_{Xe}^{TOT}}{\partial t} &= \frac{\partial y_{Xe_{U_2O}}}{\partial t} = \\ &= \nabla \cdot \left(M_{Xe_{U_2O}} y_{Xe_{U_2O}} \nabla \left(\mu_{Xe_{U_2O}} - 2\mu_U - \mu_O \right) \right), \end{aligned} \tag{3}$$

where $M_{Xe_{U_2O}}$ is the mobility of the Xe_{U_2O} cluster, $y_{Xe_{U_2O}}$ is the cluster concentration, $\mu_{Xe_{U_2O}} - 2\mu_U - \mu_O$ is the diffusion potential for the above mechanism and $-\frac{M_{Xe_{U_2O}} y_{Xe_{U_2O}}}{V_m} \nabla \left(\mu_{Xe_{U_2O}} - 2\mu_U - \mu_O \right)$ is the flux ($J_{Xe_{U_2O}}$). V_m is the molar volume. Xe atoms in trap sites without a bound U vacancy (Xe_{UO}) are immobile and thus do not contribute to diffusion and do not appear in Eq. 3. Also, the oxygen chemical potential, μ_O, disappears when the gradient is applied since it is assumed to fulfill equilibrium conditions ($\nabla \mu_O = 0$).

Diffusion of uranium via vacancy mechanisms has also been investigated by DFT calculations. For the high vacancy concentrations that may occur under irradiation, these calculations emphasize the importance of vacancy clustering (U divacancies, V_{U_2}) due to attractive vacancy binding energies and the much higher mobility of clusters compared to single vacancies. Both single vacancies and divacancies are fully charged in nearly stoichiometric UO_2, i.e. in Kröger-Vink notation the defects are V_U'''' and V_{U_2}''''''''. The diffusion of vacancies and divacancy clusters is described by:

$$\frac{\partial y_{V_U}}{\partial t} = \nabla \cdot \left(M_{V_U} y_{V_U} \nabla \left(\mu_{V_U} - \mu_U \right) \right) \tag{4}$$

and

$$\frac{\partial y_{V_{U_2}}}{\partial t} = \nabla \cdot \left(M_{V_{U_2}} y_{V_{U_2}} \nabla \left(\mu_{V_{U_2}} - 2\mu_U \right) \right), \tag{5}$$

where M_{V_U} and $M_{V_{U_2}}$ are the vacancy mobilities and $(\mu_{V_U} - \mu_U)$ and $\left(\mu_{V_{U_2}} - 2\mu_U\right)$ the corresponding diffusion potentials giving rise to the fluxes $-\frac{M_{V_U} y_{V_U}}{V_m} \nabla \left(\mu_{V_U} - \mu_U \right)$ and $-\frac{M_{V_{U_2}} y_{V_{U_2}}}{V_m} \nabla \left(\mu_{V_{U_2}} - 2\mu_U \right)$. The time evolution of the total vacancy concentration ($y_{Va}^{TOT} = y_{V_U} + 2y_{V_{U_2}}$) is expressed as the sum of these two contributions.

Finally, diffusion of U interstitials is described by:

$$\frac{\partial y_{U_I}}{\partial t} = \nabla \cdot \left(M_{U_I} y_{U_I} \nabla \left(\mu_{U_I} - \mu_{V_I} \right) \right), \tag{6}$$

where M_{U_I} is the mobility of interstitials and $(\mu_{U_I} - \mu_{V_I})$ is the diffusion potential for interstitials, which results in a flux equal to $-\frac{M_{U_I} y_{U_I}}{V_m} \nabla \left(\mu_{U_I} - \mu_{V_I} \right)$.

Eqs. 3, 4, 5 and 6 contain five independent concentration variables; $y_{Xe_{UO}}$ (concentration of Xe in vacancy trap sites), y_{V_U} (concentration of U vacancies), $y_{Xe_{U_2O}}$ (concentration of Xe trap sites with a bound vacancy), $y_{V_{U_2}}$ (concentration of uranium divacancies) and y_{U_I} (concentration of U interstitials). The concentrations of U ions on the cation sublattice and vacancies on the interstitial sublattice are dependent variables given

by site conservation. In addition to the diffusion equations above, these five variables are coupled by cluster formation and recombination reactions. Vacancies and interstitials are created and annihilated at sources and sinks, such as dislocations, grain boundaries and voids or gas bubbles. However, under irradiation, cascade events are the major source of vacancies and interstitials. All of these reactions may be captured by reaction rate equations, which, unlike the diffusion equations, do not involve any gradients. Since we are interested in diffusion under irradiation, it is not sufficient to apply equilibrium conditions for the defect concentrations. In our model the formation of Xe_{U_2O} clusters occurs according to the following reaction:

$$Xe_{UO} + V_U \rightleftharpoons Xe_{U_2O}. \tag{7}$$

The corresponding reaction rate is expressed as (Reaction 7):

$$\frac{\partial y_{Xe_{U_2O}}}{\partial t} = y_{Xe_{UO}} y_{V_U} \frac{M_{V_U}}{S^2} Z \left(\mu_{Xe_{U_2O}} - \mu_{Xe_{UO}} - \mu_{V_U}\right), \tag{8}$$

where S is the atomic jump distance for the defects, Z is the number of sites from which reaction between, e.g., Xe_{UO} and V_U, is inevitable (related to the reaction radius) and the difference in chemical potential represents the driving force for the reaction. Note that the mobility of Xe in the vacancy trap site ($M_{Xe_{UO}}$) is zero and it is thus not included in Eq. 8. In the general case the mobility factor in this equation is the sum of the mobility of the individual defects, $\frac{M_{Xe_{UO}}}{S^2} + \frac{M_{V_U}}{S^2}$, which simplifies to $\approx \frac{M_{V_U}}{S^2}$ for this special case. The driving force in Eq. 8, as well as the forces in the other reaction rate theory equations below, are formulated such that thermodynamic equilibrium is attained at steady state, $\frac{\partial y_X}{\partial t} = 0$. U interstitials may annihilate with Xe_{U_2O} clusters to form a single Xe atom in a trap site without a bound vacancy ($Xe_{U_2O} + U_I \rightleftharpoons Xe_{UO} + Va_I + U_U$), the rate of which is given by:

$$\frac{\partial y_{Xe_{U_2O}}}{\partial t} = -y_{Xe_{U_2O}} y_{U_I} \left(\frac{M_{Xe_{U_2O}}}{S^2} + \frac{M_{U_I}}{S^2}\right) \times Z \left(\mu_{Xe_{U_2O}} + \mu_{U_I} - \mu_{Xe_{UO}} - \mu_{Va_I} - \mu_{U_U}\right). \tag{9}$$

The total Xe_{U_2O} reaction rate is obtained as the sum of Eqs. 8 and 9.

The formation of U vacancy clusters (V_{U_2}),

$$V_U + V_U \rightleftharpoons V_{U_2}, \tag{10}$$

occurs with the following rate

$$\frac{\partial y_{V_{U_2}}}{\partial t} = y_{V_U} y_{V_U} \frac{2M_{V_U}}{S^2} Z \left(\mu_{V_{U_2}} - 2\mu_{V_U}\right). \tag{11}$$

The vacancy clusters may be annihilated by U interstitials ($Va_{U_2} + U_I \rightleftharpoons Va_U + Va_I + U_U$) and at sinks according to the following rate:

$$\frac{\partial y_{Va_2}}{\partial t} = K_{Va_2} - y_{Va_2} y_{U_I} \left(\frac{M_{Va_2}}{S^2} + \frac{M_{U_I}}{S^2}\right) Z(\mu_{Va_2} + \mu_{U_I} - \mu_{Va} - \mu_{Va_I} - \mu_{U_U}) - M_{Va_2} k_B T y_{Va_2} k^2_{Va_2}, \tag{12}$$

which also include a source term due to cascade events ($K_{V_{U_2}}$). In Eq. 12 k_B is the Boltzmann constant and $k^2_{V_{U_2}}$ is the strength of fixed vacancy sinks. As for the Xe_{U_2O} clusters, the total V_{U_2} reaction rate is obtained as the sum of Eqs. 11 and 12.

The formation rate of vacancies (K_{V_U}) and interstitials ($K_{U_I} = K_{V_U} + 2K_{V_{U_2}}$) is determined by the irradiation conditions. Vacancies and interstitials may be annihilated by mutual recombination or by reactions with fixed sinks such as voids, fission gas bubbles, grain boundaries and dislocations. The interstitial and vacancy sink strengths are labeled $k^2_{U_I}$ and $k^2_{V_U}$, respectively. This gives the following rate theory equations:

$$\frac{\partial y_{V_U}}{\partial t} = K_{V_U} - M_{V_U} k_B T y_{V_U} k^2_{V_U} - \left(\frac{M_{V_U}}{S^2} + \frac{M_{U_I}}{S^2}\right) \times y_{V_U} y_{U_I} \left(\mu_{V_U} + \mu_{U_I} - \mu_{Va_I} - \mu_{U_U}\right) \tag{13}$$

and

$$\frac{\partial y_{U_I}}{\partial t} = K_{U_I} - M_{U_I} y_{U_I} k^2_{U_I} - \left(\frac{M_{V_U}}{S^2} + \frac{M_{U_I}}{S^2}\right) y_{V_U} y_{U_I} \left(\mu_{V_U} + \mu_{U_I} - \mu_{V_I} - \mu_{U_U}\right). \tag{14}$$

The total V_U reaction rate is obtained as the sum of Eq. 13, the negative of Eq. 11, Eq. 8 and Eq. 9 as well as the interstitial term of Eq. 12. Similarly, the total interstitial reaction rate is given by the sum of Eqs. 6, 9 and the interstitial term of Eq. 12.

The above model does not include Xe clusters involving more than one bound U vacancy to the Xe tap site, e.g. Xe_{U_3O}. The concentration of such clusters is assumed to be low, but if their mobilities are high they may still be important for diffusion. This situation is investigated by adding the Xe_{U_3O} cluster to the rate theory model. Its formation may be described by the following reactions:

$$Xe_{U_2O} + V_U \rightleftharpoons Xe_{U_3O} \tag{15}$$

or

$$Xe_{UO} + V_{U_2} \rightleftharpoons Xe_{U_3O}. \tag{16}$$

Formation of the Xe_{U_3O} cluster competes with addition of Xe atoms to the cluster, which corresponds to nucleation of small fission gas bubbles. This process may be described by the following reaction:

$$Xe_{U_3O} + Xe_{UO} \rightleftharpoons (Xe_2)_{U_3O} + V_U \tag{17}$$

Other reactions and clusters are possible. However, the present model is not meant to be exhaustive, but rather

models the basic features of large vacancy clusters with few Xe atoms (Xe_{U_3O}, which is mobile) and the same vacancy cluster with additional Xe atoms mimicking the formation of small fission gas bubbles ($(Xe_2)_{U_3O}$, which is less mobile). The corresponding reaction rates are

$$\frac{\partial y_{Xe_{U_3O}}}{\partial t} = y_{Xe_{U_2O}} y_{V_U} \frac{M_{Xe_{U_2O}} + M_{V_U}}{S^2} Z \times \left(\mu_{Xe_{U_3O}} - \mu_{V_U} - \mu_{Xe_{U_2O}}\right), \tag{18}$$

$$\frac{\partial y_{Xe_{U_3O}}}{\partial t} = y_{Xe_{UO}} y_{V_{U_2}} \frac{M_{Xe_{UO}} + M_{V_{U_2}}}{S^2} Z \times \left(\mu_{Xe_{U_3O}} - \mu_{V_{U_2}} - \mu_{Xe_{UO}}\right) \tag{19}$$

and

$$\frac{\partial y_{(Xe_2)_{U_3O}}}{\partial t} = y_{Xe_{U_3O}} y_{V_U} \frac{M_{Xe_{U_3O}} + M_{V_U}}{S^2} Z \times \left(\mu_{(Xe_2)_{U_3O}} + \mu_{V_U} - \mu_{Xe_{U_3O}} - \mu_{Xe_{UO}}\right). \tag{20}$$

Diffusion of the Xe_{U_3O} and $(Xe_2)_{U_3O}$ clusters is modeled with diffusion equations similar to Eq. 3. The Xe_{U_3O} cluster interacts with interstitial U ions according to the reaction:

$$Xe_{U_3O} + U_I \rightleftharpoons Xe_{U_2O}, \tag{21}$$

with the reaction rate

$$\frac{\partial y_{Xe_{U_3O}}}{\partial t} = -y_{Xe_{U_3O}} y_{U_I} \frac{M_{Xe_{U_3O}} + M_{U_I}}{S^2} Z \times \left(\mu_{Xe_{U_3O}} + \mu_{U_I} - \mu_{Xe_{U_2O}} - \mu_{V_I} - \mu_{U_U}\right). \tag{22}$$

Due to the the high mobility of the Xe_{U_3O} cluster this reaction will be important.

B. Model parameters

Most of the parameters in Eqs. 3, 4, 5, 6, 8, 9, 11, 12, 13 and 14 have been calculated using DFT and empirical potentials[1]. The defect mobilities are listed in Table I. In order to obtain the chemical potentials and the differences in chemical potentials defining the driving forces, we first need to express the total free energy of the $(U_U, V_U, V_{U_2}, Xe_{UO}, Xe_{U_2O})(V_I, U_I)O_2$ system, where the parenthesis separates different sublattices and the symbols indicate the defect types that are contained on each sublattice. Xe atoms are assumed to exclusively occupy vacancy trap sites, i.e. the concentration of interstitial Xe atoms is negligible. By applying a quinary regular solution model for the cation sublattice and an ideal solution model for the interstitial sublattice as well as the gradient energy terms required to describe dissolution kinetics, the following free energy density functional is obtained:

$$\frac{G_m^{Total}(y_s, T)}{N_A} = \sum_s y_s {}^oG_s^{UO_2} + \sum_s k_B T (y_s \ln(y_s)) + \sum_{s_1, s_2, s_1 \neq s_2} {}^0L_{s_1,s_2} y_{s_1} y_{s_2} + \sum_s \frac{\epsilon_s}{2} (\nabla y_s)^2. \tag{23}$$

Here s covers all species on the cation and interstitial sublattices (U_U, Xe_{UO}, Xe_{U_2O}, V_U, V_{U_2}, U_I and V_{U_I}), y_s are the site fractions and ϵ_s the gradient energy of species s. ${}^0L_{s_1,s_2}$ are the regular solution parameters for interaction between species s_1 and s_2 on the cation sublattice (s_1 and s_2 are U_U, Xe_{UO}, Xe_{U_2O}, V_U and V_{U_2}). N_A is Avogadro's number converting the left hand side of the equation to energy per atom rather than mole (this convention will be applied throughout this work). Site conservation implies that:

$$y_{U_U} + y_{Xe_{UO}} + 2y_{Xe_{U_2O}} + y_{V_U} + 2y_{V_{U_2}} = 1 \tag{24}$$

and

$$y_{U_I} + y_{Va_I} = 1. \tag{25}$$

The ${}^oG_s^{UO_2} = {}^oH_s^{UO_2} - T{}^oS_s^{UO_2}$ terms were defined according to the defect formation (V_U, V_{U_2}, U_I) or solution (Xe_{UO} and Xe_{U_2O}) energies and entropies combined with cluster binding energies and entropies, as calculated from DFT and empirical potentials (see Table I[1]). These parameters are all functions of the $UO_{2\pm x}$ non-stoichiometry[1]. The data in Table I assumes nearly stoichiometric UO_2, but can easily be extended to other non-stoichiometries based on data presented in, e.g., Ref. 1. The Xe reference state is defined as the gas phase at 298 K and 100000 Pa. The ${}^oG_U^{UO_2}$ reference is set to 0 eV. The ${}^oG_s^{UO_2}$ parameters are constants and thus only relevant for the rate theory equations ($\nabla {}^oG_s^{UO_2} = 0$ in the diffusion equations). The regular solution parameters ${}^0L_{s_1,s_2}$ were calculated from the DFT binding energies (E_B) and the number of available binding sites (Z_B):

$${}^0L_{s_1,s_2} = \frac{Z_B}{2} E_B. \tag{26}$$

Only the most stable site for each defect was considered. The temperature dependence of the regular solution parameters (${}^0L_{s_1,s_2} = {}^0L^0_{s_1,s_2} + {}^0L^1_{s_1,s_2} T$) was set to zero (${}^0L^1_{s_1,s_2} = 0$ eV). The ${}^0L_{s_1,s_2}$ values are summarized in Table I. The values reflect the strong binding between Xe atoms and vacancies as well as that between Xe atoms themselves, which capture the tendency to nucleate fission gas bubbles. However, the present model is not optimized to capture the properties of bubbles, which is primarily a consequence of only treating U vacancies and not the O vacancies or bound Schottky defects (one U vacancy and two O vacancies) required to capture growth of bubbles. This topic is left as future work. We did not attempt to calculate the interfacial energies (ϵ_s) from either DFT or empirical potentials. Careful determination

of these parameters is also left as future work. The chemical potential differences in the diffusion and reaction rate equations are calculated from the free energy density in Eq. 23 according to:

$$\mu_A - \mu_B = \frac{\delta}{\delta y_A}\left(\int_\Omega G_m^{Total} d\Omega\right)_{y_B} = \\ = \left(\frac{\partial G_m^{Total}}{\partial y_A}\right)_{y_B} - \nabla \cdot \left(\frac{\partial G_m^{Total}}{\partial \nabla y_A}\right)_{y_B}, \quad (27)$$

where B is treated as the dependent variable and Ω is the integration volume.

The model that includes the large Xe_{U_3O} and $(Xe_2)_{U_3O}$ clusters were formulated by adding Eqs. 16 and 20 as well as the corresponding diffusion equations (Eq. 3) to the reaction diffusion model. The Xe_{U_3O} and $(Xe_2)_{U_3O}$ clusters must consequently be added to the free energy expression (Eq. 23) as well as to the site conservation expression (Eq. 24). In order to simplify the model implementation the clusters were treated as ideal constituents, which implies that all interaction parameters involving these two clusters were set to zero, which is motivated by the small cluster concentrations. The formation energies entering the reaction rate equations and cluster diffusivities are listed in Table I and obtained from DFT calculations according to the same methodology as for the smaller clusters. Because calculated values were not available, the entropies were approximated as zero.

The remaining parameters K_{V_U}, $K_{V_{U_2}}$, K_{U_I}, $k^2_{V_U}$, $k^2_{Va_2}$ and $k^2_{U_I}$ were estimated from experimental data[1,24] or treated as free parameters. Typical values are listed in Table I.

C. Numerical simulations

The diffusion and rate theory equations (Eqs. 3, 4, 5, 6, 8, 9, 11, 12, 13, 14, 16 and 20) were implemented in the MARMOT phase field code[25], which is based on the MOOSE finite element framework[26,27]. The simulations used adaptive time-stepping and adaptive meshing. In order to avoid numerical instabilities for very low concentrations, logarithm terms and their derivatives were Taylor expanded below a certain threshold value (10^{-12}).

D. Results and Discussion

1. *Simulations of effective Xe and U diffusivities in UO_2*

Both Xe and U diffusivities are functions of the vacancy concentration, which in thermodynamic equilibrium is expressed in terms of the vacancy formation energy. Ref. 1 performed this analysis for UO_2 based on the same data from DFT and empirical potentials as applied in our study (see Table I). They predicted an activation energy of 2.93 eV and a pre-exponential factor of $8.32 \cdot 10^{-12}$ m^2/s for Xe diffusion in stoichioemtric UO_2. Effective diffusivities may be calculated from our model by imposing flux boundary conditions at the left and right ends of a rectangular simulation cell and zero flux conditions at the top and bottom. By measuring the steady state concentration gradient, the effective diffusivity is obtained as:

$$D_X = -\frac{J_X}{\nabla y_X} \quad (28)$$

By performing simulations at a number of different temperatures, the activation energy and pre-exponential factor, $D_X = D_0 \exp\left(-\frac{E_a}{k_B T}\right)$, can be extracted. The results are plotted in Fig. 1 and both $D^0_{Xe} = 8.71 \cdot 10^{-12}$

Formation energies	${}^oH_s^{UO_2}$ (eV)	${}^oS_s^{UO_2}$ (k_B)
${}^oG^{UO_2}_{U_U}$	0.00	0.00
${}^oG^{UO_2}_{V_U}$	-0.19	-16.35
${}^oG^{UO_2}_{V_{U_2}}$	-0.30	7.19
${}^oG^{UO_2}_{Xe_{UO}}$	x	y
${}^oG^{UO_2}_{Xe_{U_2O}}$	$x - 1.82$	$y + 1.97$
${}^oG^{UO_2}_{Xe_{U_3O}}$	$x - 1.50$	y
${}^oG^{UO_2}_{(Xe_2)_{U_3O}}$	$2x - 6.07$	$2y$
${}^oG^{UO_2}_{V_I}$	0.00	0.00
${}^oG^{UO_2}_{U_I}$	13.20	0.00
Regular solution parameters	${}^0L^0_{s_1,s_2}$ (eV)	${}^0L^1_{s_1,s_2}$ (k_B)
${}^0L_{Xe_U,V_U}$ (eV)	-10.92	0.00
${}^0L_{U_U,V_U}$ (eV)	1.80	0.00
${}^0L_{Xe_{UO},U_U}$ (eV)	9.12	0.00
${}^0L_{Xe_{UO},V_U}$ (eV)	5.04	0.00
${}^0L_{Xe_{U_2O},V_U}$ (eV)	-6.55	0.00
${}^0L_{Xe_{U_2O},Xe_U}$ (eV)	-7.73	0.00
${}^0L_{Xe_{UO},V_{U_2}}$ (eV)	-9.51	0.00
${}^0L_{Xe_{U_2O}},V_{U_2}$ (eV)	16.49	0.00
${}^0L_{U_U,V_{U_2}}$ (eV)	4.80	0.00
${}^0L_{V_U,V_{U_2}}$ (eV)	-3.34	0.00
Kinetic parameters	D_0 (nm^2/s)	E_m (eV)
$D_{Xe_{U_2O}}$	$1.481 \cdot 10^{13}$	4.94
$D_{Xe_{U_3O}}$	$1.481 \cdot 10^{13}$	4.33
$D_{(Xe_2)_{U_3O}}$	$1.481 \cdot 10^{13}$	4.94
D_{V_U}	$7.121 \cdot 10^{11}$	4.72
$D_{V_{U_2}}$	$5.446 \cdot 10^{13}$	2.84
D_{U_I}	$1.2 \cdot 10^{12}$	4.70
Other parameters		
Z	1.0	
K (defects/U atom s)	$4.05 \cdot 10^{-6}$	
k^2_I (1/nm^2)	0.012564	
k^2_V (1/nm^2)	0.012564	

TABLE I. Bulk thermodynamic and kinetic parameters for defects in UO_2.

and $E_a = 2.94$ eV agree well with the analytical results from Ref. 1. At the lower end of the temperature range, cluster formation starts to become controlling and the diffusivity tends towards that predicted for the mobile Xe trap site (Xe_{U_2O}). The same type of simulation can be performed for the flux of U ions, which corresponds to a tracer diffusion experiment. The results in Fig. 1 gives $D_{U^*} = 5.718 \cdot 10^{-14}$ m^2/s and $E_a = 4.55$ eV, which agrees well with the analytical solution of $D_{U^*} = 5.61 \cdot 10^{-14}$ m^2/s and $E_a = 4.53$ eV derived from the data in Ref. 1 and the experimental activation energy of 4.4 eV[37]. The pre-exponential factor is underestimated compared to experiments (the experimental value is $D_{U^*} = 8.54 \cdot 10^{-11}$ m^2/s)[37]. The explanation for the latter discrepancy is unrelated to the numerical implementation and will not be further explored in this study.

In the next step we perform the same type of simulation, but introduce damage via the K_{V_U}, $K_{V_{U_2}}$ and $K_{V_{U_I}}$ parameters. Fig. 2a) plots the Xe diffusivity as function of temperature for a particular value of the damage rate ($4.05 \cdot 10^{-6}$ defects/U atom s). We simulated two different scenarios for the vacancy production; in the first we assumed only single uranium vacancies and in the second single uranium vacancies and uranium divacancies are formed with equal probability. Fig. 2a) shows that at high and low temperature the predicted diffusivities approach the intrinsic case, while in the intermediate temperature regime, the damage gives rise to irradiation enhanced diffusion. In the irradiation enhanced temperature region the effective diffusivity is slightly higher for the case when both single vacancies and divacancies are created in the damage process, but the difference is small. The analytical models capture the diffusivity well outside of the intermediate temperature range, but within this range the calculated diffusivity exceeds the analytical prediction from both the intrinsic and irradiation enhanced models. We have also investigated the effect of varying the sink strengths, defect production rates and the concentration of fission gas atoms. As expected, increasing the damage rate and decreasing the sink strength both lead to higher diffusivity in the intermediate temperature range and also extension of the irradiation enhanced range to higher temperature. The opposite conclusion applies to decreasing damage rates and inceasing sink strengths. The diffusivity is largely independent of the concentration of Xe atoms at high temperature, but below 2000 K the diffusivity increases slightly for decreasing Xe concentrations. This is a consequence of increased clustering between vacancies and Xe atoms at low Xe concentrations. In the microstructure simulations in Sec. III B 1 we treat the Xe diffusivity as independent of the concentration.

Fig. 3 plots the effective diffusivity obtained when the Xe_{U_3O} and $(Xe_2)_{U_3O}$ clusters are included. The damage rate and sink strengths are the same as in previous simulations (see Table I). Even though the concentration of Xe_{U_3O} cluster is small, its high mobility compared to Xe_{U_2O} gives a significant contribution to the diffusivity across almost the full temperature range. At the highest temperature in our simulations the diffusivity approaches the intrinsic case. Below the highest temperatures the diffusivity is controlled by cluster diffusion, primarily the Xe_{U_2O} cluster but at the lowest temperature in our simulations also the Xe_{U_3O} cluster. The temperature dependence of the diffusivity and the influence of different clusters is a function of the cluster thermodynamics, which is still under investigation. The prediction may also depend on how fast the Xe_{U_3O} and $(Xe_2)_{U_3O}$ clusters accumulate even more Xe atoms and vacancies, which would make them much less mobile. The current model does capture those processes. Nevertheless, our results suggest that under irradiation the Xe_{U_3O} clusters are important for the overall diffusivity due to their high mobility and strong binding energy.

III. XE SEGREGATION TO GRAIN BOUNDARIES

A. Model derivation

The interaction between Xe atoms and the UO_2 fuel microstructure is critical for fission gas release. In order to simulate redistribution of fission gas atoms to microstructure sinks, the interaction between fission gas atoms and the sinks must first be determined and then formulated in a continuum model suitable for coupling to the diffusion and rate theory models developed in Sec. II. We have investigated segregation of Xe atoms to three different grain boundary types, $\Sigma5$ tilt, $\Sigma5$ twist and a high angle random boundary. Nerikar *et al.* calculated grain boundary segregation energies for Xe in UO_2 using atomistic simulations with the interatomic interactions described by empirical potentials[22]. They provide data on the segregation energy as function of the distance from the boundary as well as the distribution of segregation sites at the boundary. The segregation energy is defined as the energy difference between a Xe atom occupying a bulk position far away from the grain boundary and a Xe atom positioned within the grain boundary. The assumption that Xe atoms reside in a single U vacancy ignores the fact that Xe atoms are believed to occupy trap sites consisting of one U and either one or two additional O vacancies in stoichiometric UO_2[19,30,31]. Nevertheless, the relative energies obtained from this assumption should capture the segregation trends correctly, which was also confirmed by performing a couple of spot checks for Xe occupying a bound Schottky defect (one U and two O vacancies).

The segregation properties are unique for each type of grain boundary, as illustrated in Fig. 4. This conclusion refers to both the maximum sink strength, i.e. the most negative segregation energy, and the distribution of segregation sites as function of distance from the centre of the grain boundary. The random boundary is the strongest Xe sink, followed by the $\Sigma5$ tilt and $\Sigma5$ twist bound-

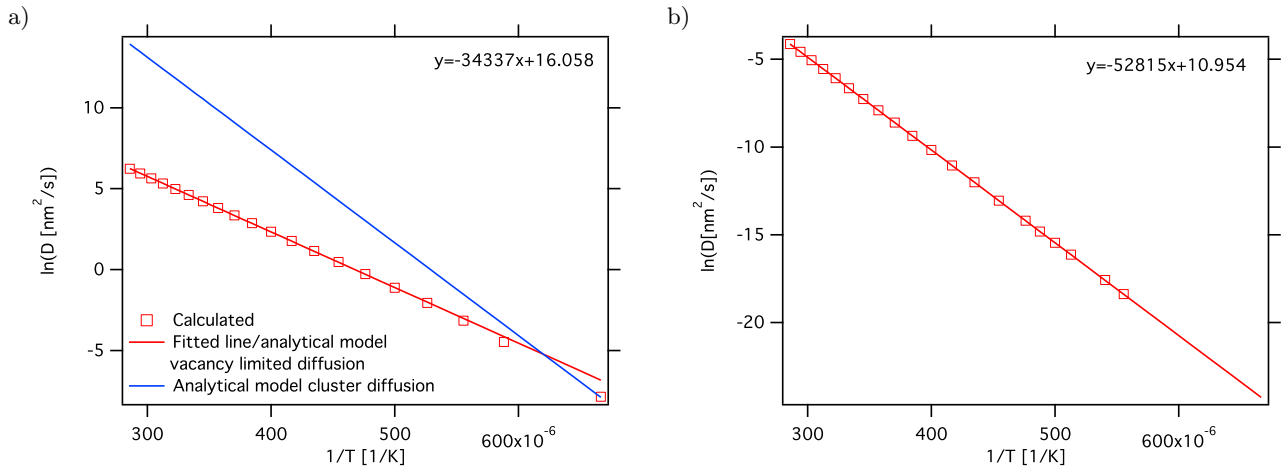

FIG. 1. The Xe (a) and U (b) diffusivity as function of temperature under intrinsic conditions calculated from MARMOT simulations.

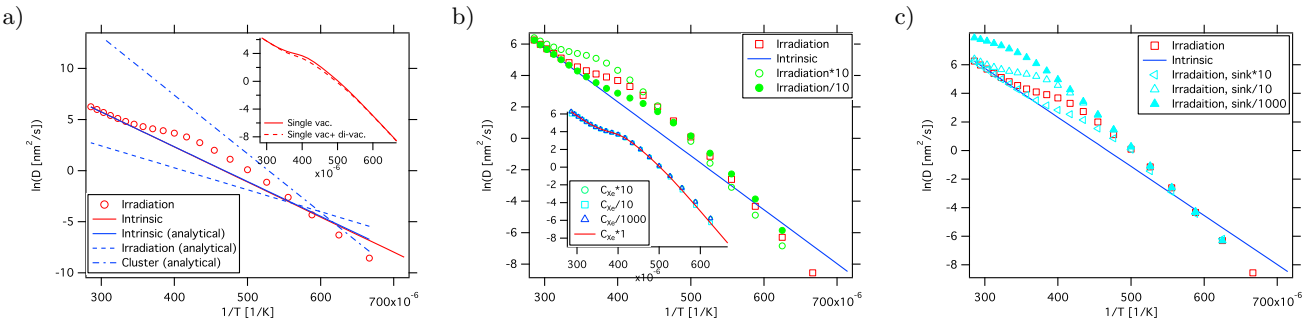

FIG. 2. a) The Xe diffusivity under irradiation conditions compared to the intrinsic diffusivity and the corresponding analytical expressions derived in Ref.[1]. b) The effect of increasing and decreasing the defect production by factors of 10 compared to the simulation in a). The inset shows how the effective Xe diffusivity depends on the concentration of Xe atoms, measured in factors of 10 compared to the simulation in a). c) The effect of increasing and decreasing the sink strength by factors of 10 compared to the simulation in a).

aries. Segregation of large atoms such as Xe is often described in terms of elastic interactions, i.e. the extra volume found at the grain boundary attracts the large Xe atoms by reducing the total strain of the system. This approach was, for example, applied in phase-field simulations by Hu *et al.*[11]. Close to the boundary core this description is expected to become less accurate. Nerikar *et al.* attempted to map the Xe segregation properties onto the strain obtained from atomistic simulations, but, although some correlation was found, it was difficult to quantitatively predict the segregation energy from the local strain[22].

Fig. 5 plots the (relative) segregation energy as function of the Xe fraction in the boundary region. This quantity was derived by independently filling available Xe trap sites, starting from the most favorable one, up to a certain site fraction and the segregation energy for this concentration is then defined as the segregation energy of the next empty Xe site. Fig. 5 illustrates that the segregation energy starts rising almost exponentially. The segregation model neglects any explicit Xe-Xe interactions and they are rather assumed to be the same as in the bulk.

For application in continuum models, the atomistic segregation data summarized in Figs. 4 and 5 are represented by fits to appropriate functions. The following equation was applied for the concentration dependent Xe segregation energy density, $E_m^{Xe,gb}(y_{Xe}^{TOT}, r)$:

$$\frac{E_m^{Xe,gb}(y_{Xe}^{TOT}, \vec{r})}{N_A} = \sum_{i,j} \int_0^{y_{Xe}^{TOT}} 2\left(C_i - g_i(y'_X)\right) f_{ij}(r_{ij}) dy'_X, \tag{29}$$

where

$$f_{ij}(r_{ij}) = \frac{1}{1 + \exp\left(-r_{ij}^2/k_i^2\right)} - 1 \tag{30}$$

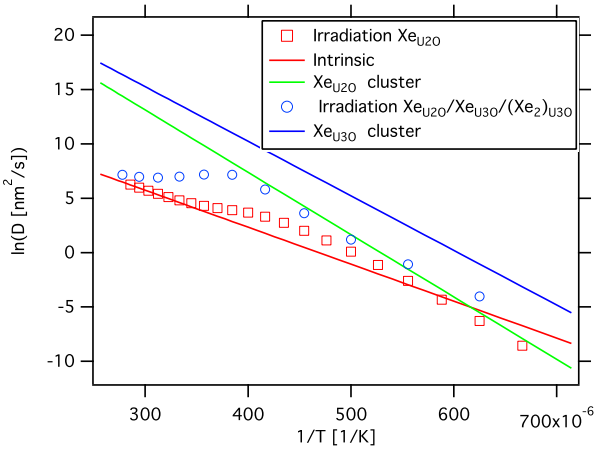

FIG. 3. The effective Xe diffusivity under irradiation conditions, comparing the diffusivity with and without the large Xe_{U_3O} and $(Xe_2)_{U_3O}$ clusters. The intrinsic diffusivity as well as the cluster diffusivities are also shown.

and

$$g_i(y_{Xe}^{TOT}) = m_i ln\left(100 y_{Xe}^{TOT} + \exp\left(\frac{-b_i}{m_i}\right)\right) + b_i. \quad (31)$$

$E_m^{X,gb}(y_{Xe}^{TOT}, \vec{r})$ is the total or integrated segregation energy as function of the (projected) distance from the grain boundary (r_{ij}) and the local (total) Xe concentration y_{Xe}^{TOT} on the cation sublattice. The i index covers different types of sinks (e.g. different types of grain boundaries) and the j index covers all sinks of a specific type i (e.g. $\Sigma 5$ tilt boundaries). C_i measures the dilute limit sink strength, g_i its concentration dependence and f_{ij} its spatial interaction range. The function $f_{ij}(r_{ij})$ describes the (normalized) segregation energy in the dilute limit, which is defined by the most negative segregation energy among all the grain boundary segregation sites available at a certain distance from the centre of the boundary. The most negative segregation energy is used for normalization (note that the normalization constant is in fact twice the lowest segregation energy, $2C_i$). In Eq. 30 the parameter k_i determines the slope of the Xe grain boundary interaction range. For each type of grain boundary the k_i parameter was fitted to the data in Fig. 4. The $g_i(y_{Xe}^{TOT})$ term (Eq. 31) describes the concentration dependence (y_{Xe}^{TOT}) of the segregation energy and the b_i and m_i parameters were fitted to the atomistic data in Fig. 5. Note that the integral in Eq. 29 measures the total segregation energy as function of the Xe fraction rather than the incremental change expressed by $g_i(y_X)$ alone. Any contributions that originate from entropy differences between bulk and grain boundaries are presently ignored. The segregation energy is assumed to be independent of temperature, which ignores the statistical distribution between segregation sites expected at high temperature.

Table II summarizes the fitted k_i, b_i and m_i values as well as the direct calculations of C_i for each grain boundary type. The quality of the $f_{ij}(r_{ij})$ and $g_i(y_X)$ fits is illustrated in Figs. 4 and 5. For $\Sigma 5$ tilt boundaries the deviation between data points and the fitted curve originates from the presence of an electrostatic field that would require a different functional form of the f_{ij} interaction range or explicit calculation of electrostatic interactions to give optimal results. Improved representation could in principle be achieved by changing the r_{ij} exponent from 2 to 1 or some non-integer value in Eq. 30. The $g_i(y_X)$ fits were performed for data points up to the concentration level indicated by the fitted red lines in Fig. 5. The upturn occurring beyond this point is ignored. This approximation has no influence on the actual simulation results since the current description still captures the saturation point for the local concentration field and, in particular, once fission gas bubble or void formation is incorporated, this process will be initiated well before reaching the local concentration limit.

In our simulations the grain boundary network is represented by a phase field model in which each grain i is described by an order parameter ϕ_i. $\phi_i = 1$ within this grain and zero in all other grains. It varies continuously from one to zero over the boundary. At a point on a boundary, several order parameters have values between zero and one. In the phase field description the sum in Eq. 29 is over the number of possible pairings between order parameters with values greater than zero. The index i denotes the properties of the grain boundary type defined by the current order parameter pair. The spatial interaction is defined as $f_i = 8\Phi_i$, where $\Phi_i = \phi_j^2\phi_k^2$. Here ϕ_j and ϕ_k are the current order parameter pair. Grain boundary triple junctions require special attention, since direct application of the above model would render them weaker sinks than regular grain boundaries. The correct properties are recovered by scaling the phase field variables by $\phi_i + \phi_j$ whenever more than two phase field variables have non-zero values.

The complete thermodynamic model for Xe segregation to grain boundaries in UO_2 is obtained as the sum of Eqs. 23 and 29. The segregation dynamics is obtained by calculating the driving forces or differences in chemical potentials from the sum of Eqs. 23 and 29 rather than Eq. 23 alone.

In order to describe the complete diffusion problem we should also treat segregation of vacancies and interstitials, however because the time-scale of these processes are quite different from the fission gas segregation we will simplify our model by assuming that these concentrations are given by the steady state solution to the reaction rate equations. This is supported by the fact that unlike Xe atoms the interstitial and vacancy defects will quickly be annihilated at the boundary and resolving these processes in detail will complicate the simulation of Xe diffusion.

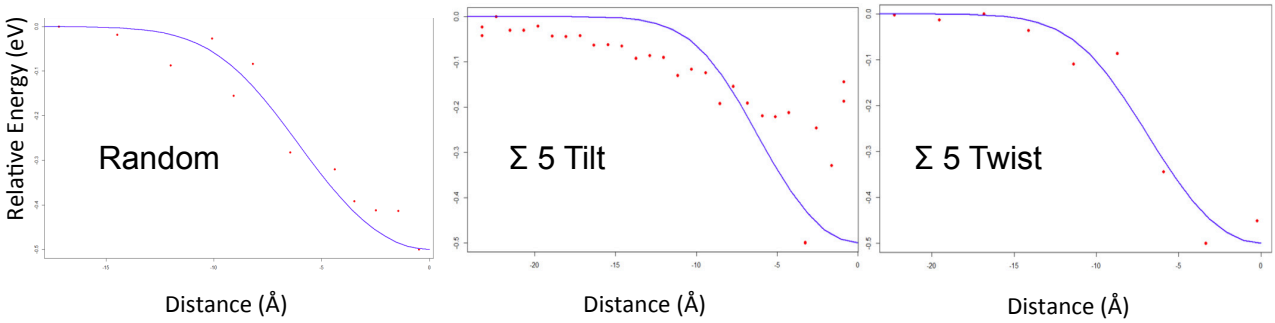

FIG. 4. The Xe segregation energy as function of the distance from the centre of the grain boundary for three different boundary types, Σ5 tilt, Σ5 twist and a high angle grain boundary classified as random (blue lines and symbols). The solid blue lines illustrate Eq. 29 without the $g(y_X)$ term (no concentration dependence) fitted to the lowest segregation energy as function of distance from the boundary.

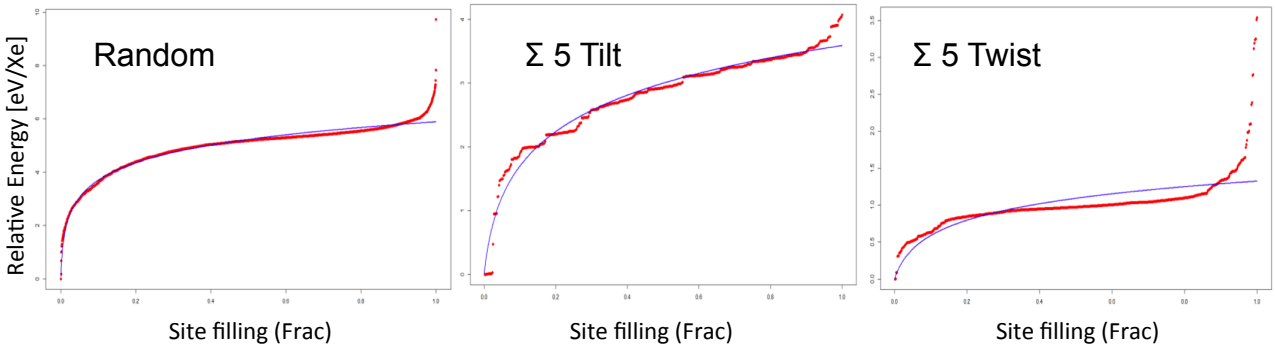

FIG. 5. The concentration dependence of the Xe segregation energies (blue lines and symbols). The solid red lines illustrate Eq. 31 fitted to the calculated data.

Grain boundary type	C_i (eV)	k_i (nm)	b_i	m_i
Σ5 tilt	3.55	0.611	-0.69599	0.93328
Σ5 twist	0.66	0.946	-0.25883	0.33972
Random	4.81	0.597	1.422386	0.94839

TABLE II. Fitted or calculated C_i, k_i, b_i and m_i parameters for Xe segregation to different grain boundary types.

B. Results and discussion

1. *Xe segregation to grain boundaries in UO_2*

Xe redistribution was simulated for three bicrystal microstructures, with a Σ5 twist, Σ5 tilt and random grain boundary, respectively. Instead of solving the full set of diffusion equations describing diffusion of Xe, interstitials and vacancy clusters, only Xe atoms are treated according Eqs. 3 (diffusion) and 29 (segregation). The diffusivity in Eq. 3 is obtained by first calculating the effective diffusivity for the relevant condition according to Sec. II D 1 and the mobility in Eq. 29 is obtained from the diffusivity as

$$M = \frac{D}{k_B T}. \tag{32}$$

First simulations are performed with the ${}^0L$ parameter set to zero. The steady-state distribution for intrinsic conditions with initial homogeneous Xe concentration of $y_{Xe} = 0.001$ at 2000 K are shown in Fig. 6. The grain size was 40 nm and the simulations were performed in a 1D configuration. Fig. 7 plots the highest Xe concentration at the core of each grain boundary as function of time for both intrinsic and radiation-enhanced conditions at 2000 K and at 1600 K. The unique behavior of the different grain boundary types is obvious in both Figs. 6 and 7. As expected, irradiation increases the rate of Xe segregation, but the difference compared to the intrinsic case is not very significant. The highest Xe concentration is reached for Σ5 tilt and the random boundary, followed by the Σ5 twist boundary. The latter has significantly lower maximum concentration. The Σ5 tilt boundary thus seems to be a stronger sink than the random boundary, despite having a lower segregation energy (see Table II). For very short times the random boundary attracts more Xe, but due to the slower (with respect to y_{Xe}) increase in the concentration term, $g_i(y_{Xe})$, the Σ5 tilt boundary eventually attracts the most Xe. The sink strength balance between these two grain boundaries is a function of the concentration of Xe. Simulations were also performed for the DFT calculated value of ${}^0L = 9.12$ eV. These results are illustrated in Fig. 8. It is clear that

for all boundaries segregation is increased for ${}^0L = 9.12$ eV.

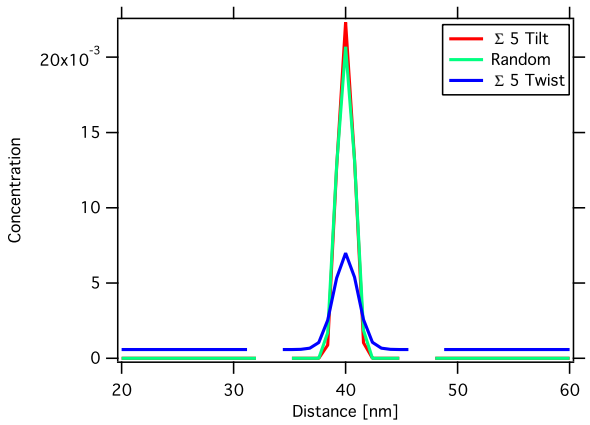

FIG. 6. Steady-state Xe distribution in a bicrystal containing a random, Σ5 tilt or Σ5 twist grain boundary. The domain size is 40×5 nm, but only visualized in the x direction. The simulations were performed for intrinsic conditions at 2000 K. The initial state was a homogeneous distribution of Xe ($y_{Xe} = 0.001$).

In order to demonstrate the importance of considering the grain boundary character, we performed simulations on a simplified 2D nanocrystalline microstructure consisting of hexagonal grains with a distribution of different grain boundary types. The simulation was performed at 2000 K for an initial concentration of $y_{Xe} = 0.001$. The size of the simulation domain is 75×65 nm and periodic boundary conditions were imposed. Fig. 9a) shows the steady state solution for ${}^0L = 0.0$ eV and b) for ${}^0L = 9.12$ eV. Finally, Fig. 9c) demonstrate that the adaptive meshing capability enables solution of the problem for a more realistic grain size (750×650 nm). The difference between the grain boundary types follow the same trend as for the bicrystal simulations. Note the drastic difference in the Xe concentration between the tilt and twist grain boundaries, which will result in preferential bubble nucleation and growth. Future work will expand this model to include bubble nucleation and growth, and investigate this effect in more detail.

IV. CONCLUSIONS

Continuum models for diffusion of xenon (Xe), uranium (U) vacancies and U interstitials in UO_2 were derived for both intrinsic conditions and under irradiation. The mechanistic diffusion models were based on results from density functional theory (DFT) and empirical potential calculations[1], which were also used for determining the model parameters. The diffusion models were implemented in the MARMOT phase field code. Effective Xe diffusivities were calculated for a range of irradiation and microstructure conditions by solving the complete set of diffusion and rate equations. Radiation-enhanced diffusion occurs at intermediate temperature ($1785 < T < 2860$ K), while at low and high temperatures the diffusivity is given by the intrinsic values. At low temperature ($T < 1785$ K) cluster formation governs the diffusivity for both intrinsic and irradiation conditions. The effective radiation enhanced diffusivity is increased when the large Xe_{U_3O} cluster is considered. Even though this cluster only occurs in small concentrations, its high mobility leads to increased diffusivity for an extended temperature range. Intrinsic conditions are only recovered above 3500 K. We are continuing to investigate the impact of large Xe and Va vacancy clusters on the effective diffusivities. Segregation of Xe to grain boundaries was described by combining the bulk diffusion model with a model for the interaction between Xe atoms and three different grain boundaries in UO_2 (Σ5 tilt, Σ5 twist and a high angle random boundary), as derived from atomistic calculations. The simulations capture the segregation of Xe to grain boundaries and the unique characteristics of different boundary types clearly emerge from these simulations. For short time scales random boundaries are the strongest sinks for Xe, but when the local Xe concentration increases the Σ5 boundary tilt overtakes the random boundary as the strongest sink. The Σ5 twist boundary attracts significantly less Xe than the other two cases.

[1] D. A. Andersson and P. Garcia and X.-Y. Liu and G. Pastore and M. Tonks and P. Millett and B. Dorado and D. R. Gaston and D. Andrs and R. L. Williamson and R. C. Martineau and B. P. Uberuaga and C. R. Stanek, J. Nucl. Mater. **451**, 225 (2014).

[2] A. H. Booth, A method of calculating gas diffusion from UO_2 fuel and its application to the X-2-f test, Technical Report AECL 496 CRDC-721, Atomic Energy of Canada Limited (1957).

[3] M. V. Speight, Nucl. Sci. Eng. **37**, 180 (1969).

[4] K. Forsberg and A. R. Massih, J. Nucl. Mater. **135**, 140 (1985).

[5] K. Forsberg and A. R. Massih, J. Nucl. Mater. **127**, 141 (1985).

[6] K. Forsberg and A. R. Massih, Modelling Simul. Mater. Sci. Eng. **15**, 335 (2007).

[7] D. D. Lanning, C. E. Beyer and C. L. Painter, "FRAPCON-3: Modifications to Fuel Rod Material Properties and Performance Models for High-Burnup Application" (1997).

[8] M.S. Veshchunov and V.D. Ozrin and V.E. Shestak and V.I. Tarasov and R. Dubourg and G. Nicaise, Nucl. Eng. Des. **236**, 179 (2006).

[9] M.S. Veshchunov and R. Dubourg and V.D. Ozrin and V.E. Shestak and V.I. Tarasov, J. Nucl. Matrer. **362**, 327

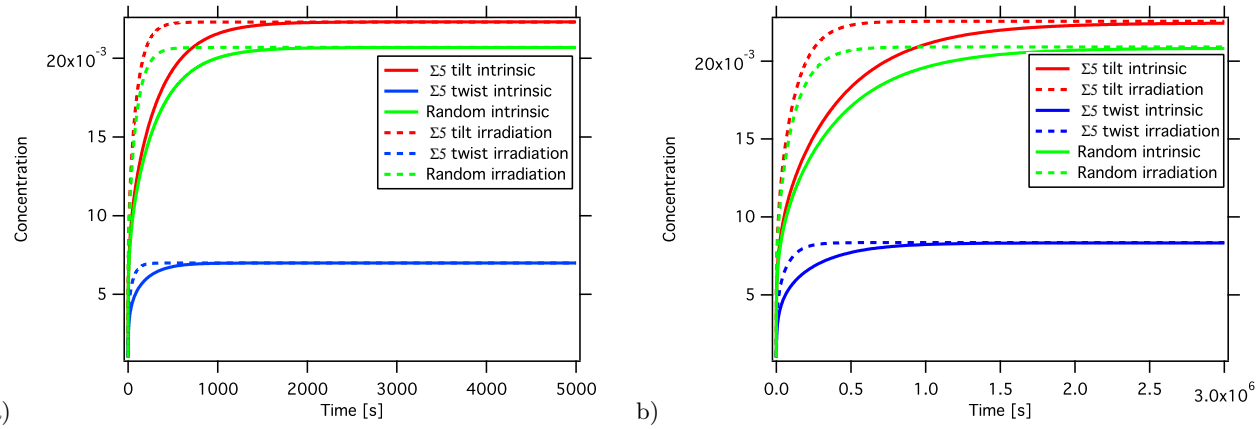

FIG. 7. The highest Xe concentration at the core of the grain boundary as function of time for both intrinsic and radiation-enhanced conditions. The initial state was a homogeneous distribution of Xe ($y_{Xe} = 0.001$). a) The simulation temperature was 2000 K and b) 1600 K.

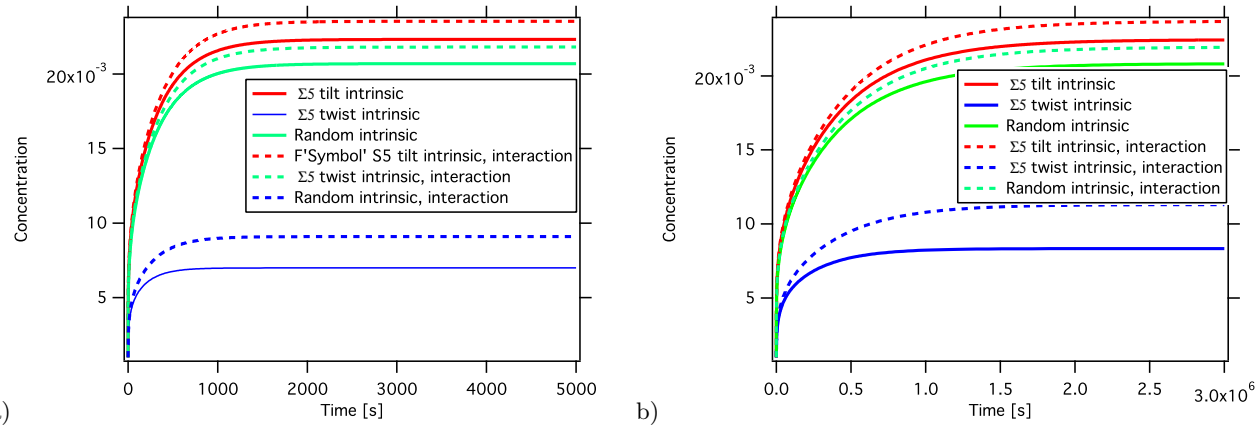

FIG. 8. The highest Xe concentration at the core of the grain boundary as function of time for intrinsic condition with the ${}^0L = 0.0$ eV and ${}^0L = 9.12$ eV. a) The simulation temperature was 2000 K and b) 1600 K.

(2007).
[10] M.S. Veshchunov, J. Nucl. Matrer. **277**, 67 (2000).
[11] S.-Y. Hu, C. H. Henager Jr, H. L. Heinisch, M. Stan, M. I. Baskes and S. M. Valone, J. Nucl. Mater. **392**, 292 (2009).
[12] S.-Y. Hu, C. H. Jr. Henager, Acta Mater. **58**, 3230 (2010).
[13] Y. L. Li, S. Y. Hu, X. Sun, F. Gao, C. H. Henager Jr and M. Khaleel, J. Nucl. Mater. **407**, 119 (2010).
[14] P. C. Millett, D. Wolf and T. Desai, J. Appl. Phys. **104**, 033512 (2008) .
[15] P. C. Millett, A. El-Azab, S. Rokkam and M. Tonks and D. Wolf, Comput. Mater. Sci. **50**, 949 (2011).
[16] P. C. Millett, A. El-Azab and D. Wolf, Comput. Mater. Sci. **50**, 960 (2011).
[17] P. C. Millett and M. Tonks, Curr. Opin. Solid State Mater. Sci. **15**, 125 (2011).
[18] X.-Y. Liu, B. P. Uberuaga, D. A. Andersson, C. R. Stanek, and K. E. Sickafus, Appl. Phys. Lett. **98**, 151902 (2011).
[19] D. A. Andersson, B. P. Uberuaga, P. V. Nerikar, C. Unal and C. R. Stanek, Phys. Rev. B **84**, 054105 (2011).
[20] R. G. J. Ball and R. W. Grimes, J. Chem. Soc., Faraday Trans. **86**, 1257 (1990).
[21] C. R. A. Catlow, Proc. R. Soc. Lond. A **364**, 473 (1978).
[22] P.V. Nerikar, D. C. Parfitt, L. A. Casillas Trujillo, D. A. Andersson, C. Unal, S. B. Sinnott, R. W. Grimes, B. P. Uberuaga and C. R. Stanek, Phys. Rev. B **84**, 174105 (2011).
[23] J. A. Turnbull, J. Nucl. Mater. **50**, 63 (1974).
[24] J. A. Turnbull, C. A. Friskney, J. R. Findlay, F. A. Johnson and A. J. Walter, J. Nucl. Mater. **168**, 168 (1982).
[25] M. R. Tonks and D. Gaston and P. C. Millett and D. Andrs and P. Talbot, Comput. Mater. Sci. **51**, 20 (2012).
[26] D. Gaston, G. Hansen, S. Kadioglu, D. Knoll, C. Newman, H. Park, C. Permann and W. Taitano, J. Phys.: Conf. Ser. **180**, 012012 (2009).
[27] M. Tonks, D. Gaston, C. Permann, P. Millett, G. Hansen and D. Wolf, Nucl. Eng. Design **83**, 2877 (2010).
[28] D. McLean, Grain Boundaries in Metals (London: Oxford University Press), 1957.
[29] M. P. Seah, J. Phys. F: Metal Phys., **10**, 1043 (1980).
[30] R. G. J. Ball and R. W. Grimes, Chem. Soc., Faraday Trans. **86**, 1257 (1990).
[31] P. V. Nerikar, X.-Y. Liu, B. P. Uberuaga, C. R. Stanek, S. R. Phillpot and S. B. Sinnott, J. Phys.-Condens. Mat. **21**, 435602 (2009).

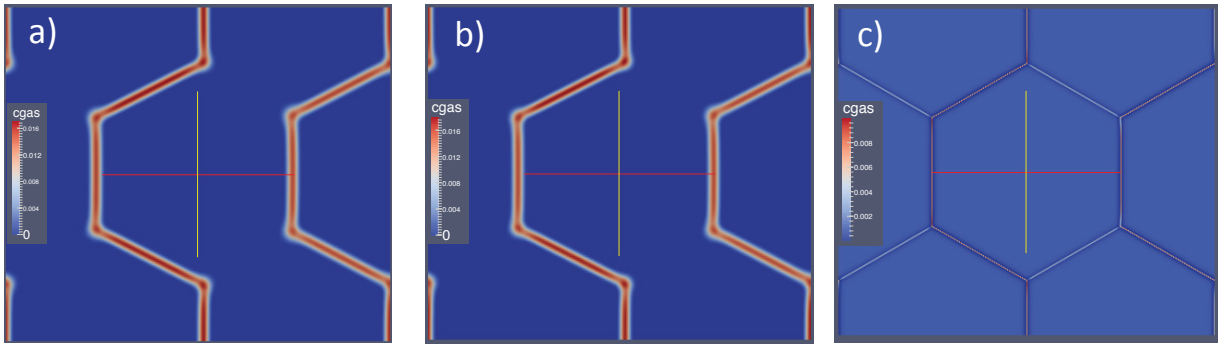

FIG. 9. a) Xe distribution for a microstructure composed of random, Σ5 tilt and Σ5 twist grain boundaries. The Xe-Xe interaction parameter was set to 0 (^0L=0 eV, ideal solution). b) The same as a), but with the Xe-Xe interaction parameter set to 9.32 (^0L=9.32 eV, regular solution). For both cases the domain size is 75 × 65 nm and the initial state was a homogeneous distribution of Xe ($y_{Xe} = 0.001$). c) The same as in a) but with a larger domain size (750 × 650 nm).

[32] P. Nerikar, C. R. Stanek, S. R. Phillpot, S. B. Sinnott and B. P. Uberuaga, Phys. Rev. B **81**, 064111 (2010).

[33] J. W Cahn, Acta Mater. **9**, 795 (1961).

[34] Hj. Matzke, J. Chem. Soc., Faraday Trans. 2 **83**, 1121 (1987).

[35] D. R. Olander, Fundamental Aspects of Nuclear Reactor Elements, NTIS, ERDA, 1975.

[36] N. Moelans, B. Blanpain, P. Wollants, CALPHAD **32**, 268 (2008).

[37] A. C. S. Sabioni, W. B. Ferraz, and F. Millot, J. Nucl. Mater. **257**, 180 (1998).